

Spin Relaxometry of Nitrogen-Vacancy Centers in Diamond as a Function of Diamond Size

Pravan Chakravarthy (Department of Physics, University of Chicago), *SUNFEST Fellow*
Rebecca Fishman (Department of Physics and Astronomy, University of Pennsylvania), *mentor*
Lee C. Bassett (Department of Electrical and Systems Engineering, University of Pennsylvania), *advisor*

Abstract—The nitrogen-vacancy (NV) center is a point defect in diamond that has many applications in quantum computing, biomedicine, and other fields. Its chemical and physical properties enable it to function as a spin qubit for quantum information processing. NV centers can also be utilized in improving the quality of nanoscale medical imaging, particularly important to which is the spin-lattice relaxation time (T_1) of a given quantum system. In this research, T_1 measurements on nanodiamonds (NDs) are conducted and relaxation rates $1/T_1$ are analyzed as a function of ND size. An increase in size is found to correspond with a decrease in relaxation rate, and is compared to a previous study. The results shed some light into the optimal choice of size for computing and biosensing applications, but leave plenty of room for further research.

Index Terms—biosensors, dynamic light scattering, light absorption, magnetic sensing, nanodiamonds, nitrogen-vacancy centers, quantum computing, quantum optics, qubit, spin relaxometry, ultraviolet-visible spectroscopy

INTRODUCTION

Nitrogen-vacancy (NV) centers in diamond consist of a nitrogen atom and an adjacent vacancy substituted for two carbon atoms in the crystal lattice of diamond, a point defect that is enabled because of diamond's large (5.5 eV) band gap [1]. The NV center, specifically its negative charge state, is a highly studied quantum system for a variety of reasons. An NV center can be used to read out the nuclear spin state of the nitrogen and surrounding carbon atoms, meaning that many computations could potentially be performed at once, reducing the number of resources needed to process quantum information [2]. NV centers can also remain largely unperturbed by their environment due to other properties of diamond, like its aforementioned wide band gap and weak spin-orbit coupling interactions. These abilities can be very useful for increasing coherence times for information storage. Thus, understanding the properties of NV centers as spin qubits (spin-based storage units at the quantum level) may bring forth important advances in quantum computing [1, 3].

Another application of NV centers is in developing quantum biosensors. Current magnetic

resonance imaging (MRI) technology, which depends on excitations of spin states, is only reliable for large ensembles of spin systems: at the micrometer or nanometer scale, it is not sensitive enough to provide a clear image [3, 4]. NV centers in nanodiamonds (NDs) can help in this regard because their small size (and ability to be placed close to the ND's surface) satisfies the need to increase resolution by more finely detecting magnetic and electric fields. NV centers exhibit a property called optically detected magnetic resonance (ODMR), which means that the spin state of the NV center can be read out optically (by using light to excite the quantum system). This property has only been observed in a few other defects [2, 5].

Important to computing, biosensing, and other applications is the manipulation of the center's spin states. One process that accomplishes this particularly with respect to medical imaging specifically is called spin relaxometry, which can be used to quantify the system's spin-lattice relaxation time (T_1). This time varies depending on small differences in the system, which is important to account for because of the dependence of current biosensing technologies on measuring spin states. T_1 also contributes to the coherence of a quantum system, or how long information can stably be held in a qubit [6]; in biosensing, longer T_1 times mean better sensitivity to the immediate environment [7].

This research aims to determine whether the size of a nanodiamond affects its T_1 time. In the process, certain properties of the diamonds, like light absorption and size distribution, are determined. T_1 measurements are done on suspended fluorescent nanodiamonds with an inverted confocal microscope, using different sequences of optical pulses. They are then fit to an exponential curve of fluorescence (measured by counting photons) as a function of how long the system is kept in the dark [4, 5]. Size is found to positively correlate with T_1 in each analysis performed. The results are also favorably compared to two models produced by Tetienne *et al.* (2013), simulating the best and worst cases of placement of single NVs within an ND. With further exploration, this research could help illuminate optimal qualities of NV centers and nanodiamonds for a potential quantum biosensor.

BACKGROUND

A. Brief overview of NV centers in biomedicine

NVs in diamond have many other appealing properties for biosensor development beyond precise magnetic field detection and ODMR. Both NVs and diamond are inert and nontoxic, meaning that NDs can be brought very close to a sample (in some studies they have even been put inside cells). This is very important because for many living samples, magnetic field strength decreases very rapidly as distance increases. NDs are also conveniently dispersible in solution, and remain stable and measurable at room temperature or higher [3, 5, 7]. In addition to potential usefulness in other magnetic imaging techniques such as microscale nuclear magnetic resonance (NMR) spectroscopy, NV centers also have applications in quantum thermometry, enabling increased sensitivity to temperature-related phenomena *in vivo* that could potentially offer insights into how heat affects cell and organism growth [5, 6]. Outside of sensing and imaging, NV centers may even be used as platforms for drug, gene, or protein delivery [8].

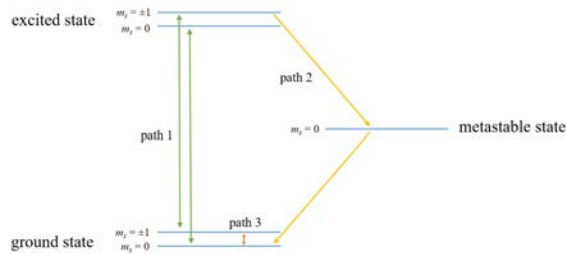


Figure 1. Energy level diagram of the nitrogen-vacancy center.

B. Energy levels and relaxation processes of the NV center

The NV center's energy levels and the possible types of transitions between them are depicted in Figure 1. The ground state and excited state are both electron spin triplets with spin angular momentum (m_s) values of 0 and ± 1 . When the system is excited, electrons radiatively decay from each excited state to its respective ground state (path 1), but non-radiative decay also occurs from the $m_s = \pm 1$ excited state to a metastable $m_s = 0$ singlet state, which then preferentially decays to the $m_s = 0$ ground state (path 2). Therefore, after some time the system is very likely (near 100% probability) to have fully relaxed into the $m_s = 0$ state. (This process is called "initialization" and allows the quantum spin state to be specifically set.) Then, the light in the system is turned off, and the transitions to the excited state cease. All the particles end up in the $m_s = 0$ ground state, and begin to follow path 3, "relaxing" from $m_s = 0$ to $m_s = \pm 1$ [4, 5]. Thus, after some time, the probability of the system being in $m_s = 0$ decays from near 1 to about $\frac{1}{3}$ (by virtue of there being 3 spin states). T_1 , the spin-lattice

relaxation time, and the related relaxation rate $1/T_1$, are values that indicate how quickly that process takes.

C. Measuring other properties of NDs

Though nanodiamond size estimates were specified by the manufacturer, it is still important to take measurements of the size distributions of the many particles suspended in the ND solution. This size measurement in turn requires evaluating how much the samples absorb light. Absorption, which is measured using ultraviolet-visible spectroscopy (UV-Vis), helps quantify how fluorescent the diamonds are for different wavelengths of light, and also helps determine the density of NV centers in the diamond suspension [9]. Used to measure size distribution is dynamic light scattering (DLS), a process that describes the Brownian motion of suspended particles, which can be used to measure the particles' distance from each other as a function of time, and therefore the particles' size [10]. Furthermore, the NDs' size distribution contains information beyond just size, such as density and cohesion, all of which factor into fluorescence.

METHODS



Figure 2. Nanodiamond suspensions, arranged by ND size from smallest to largest. Note the increasing opacity as size increases (particularly important for predicting UV-Vis outcomes).

A. Overview

The nanodiamonds are first characterized via measurement of light absorption. Next, their size distributions are measured and compared to the size specified by the manufacturer. The T_1 measurements are conducted using a series of pulses of light from a confocal microscope setup, which manipulate the spin states of the NV centers. These results come in the form of photon counts as a function of pulse delay time, and are fit to an exponential curve; T_1 and other coefficients are extracted from this fit.

B. Nanodiamond characterization

1) ND details

Fluorescent, carboxylated ND suspensions in deionized water were purchased from Adámas Nanotechnologies. NDs are milled using the high-pressure, high-temperature (HPHT) method, and their labelled sizes range from 10 to 90 nanometers in increments of 10 nanometers. As seen in Figure 2, the solutions vary in color

and opacity, and therefore differences in light absorption were expected.

2) UV-Vis measurements

UV-Vis measurements were taken using a Cary 4000 spectrophotometer from Agilent Technologies, within the 200-1000 nanometer range. Scan controls specified in the measurement include a 0.1 second average measurement time, a 1 nanometer data interval, and a 600 nanometer/minute scan rate.

3) DLS measurements

DLS measurements were taken using a Zetasizer Nano light scattering system manufactured by Malvern Panalytical. The ND suspensions were diluted to a concentration of 975 parts Milli-Q water to 25 parts diamond solution. Each dilution was measured 3 times, with each measurement consisting of 11 ten-second runs; the measurements were taken at a temperature of 25°C with a prior equilibration time of 60 seconds. Prior to measurement each sample was sonicated for 4 to 5 minutes between 25 and 35 degrees Celsius. Measurements required the sample's absorption at 630 nanometers (the wavelength of the light used by the instrument) as well as its refractive index; the former was gathered from UV-Vis measurements while the latter was taken from the accepted value of the refractive index of diamond (2.42). The result comes out as two size distributions: one based on the fluctuations of intensities of the particles (the "intensity" measurement) and one based on the number of molecules detected of each size (the "number" measurement) [10]. The raw data (in Figure 20) consists of various size bins (which increase exponentially in width), along with the percentage of particles found to occupy each bin for each measurement. For the remainder of the analysis, this data was used directly via weighted averages and standard deviations; however, the data could also be fit to a bell curve, and averages and errors can be extracted from its coefficients.

C. T_1 data collection

T_1 times are measured via fluorescence intensity and an inverted confocal microscope with 532-nm laser excitation. After the light beam is properly aligned and focused to the center of the sample, the laser path is routed to an avalanche photodiode (APD) detector, which collects data on photon counts as a function of time. This counts vs. time number was set to about 250,000 for each sample; it can be regulated by adjusting the laser power, as well as the setting of the optical density (OD) wheel.

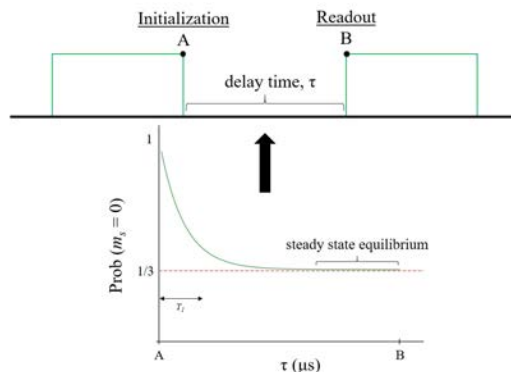


Figure 3. Diagram of an example pulse in the T_1 setup, with an illustrative exponential decay during the delay time.

The T_1 measurements themselves are obtained through a set of pulse sequences, where the light is turned off and on in specifically timed and ordered pairs of short bursts (Figure 3). When the light is on before point A, the dominant paths taken by the system are paths 1 and 2, as shown in Figure 1; at point A, when the laser is turned off, the system has been initialized. Between A and B, the dominant path taken by particles is path 3, and the probability of the system being in the $m_s = 0$ state decreases exponentially with time, reaching a steady-state equilibrium at B. The delay times between A and B vary from sequence to sequence, being as low as 150 nanoseconds and as high as 9 milliseconds. After B is reached, the light is turned back on and the spin state is read out via photon counting. The NV center exhibits spin-dependent fluorescence: if the system is in $m_s = 0$, then the radiative path 1 is more likely, meaning more photons will be counted, but if the system is in $m_s = \pm 1$, then the non-radiative path 2 is more likely, meaning fewer photons will be counted. Thus, the brightness of the system (via photon detection) is directly correlated with the probability of being in the $m_s = 0$ state, and will experience a very similar decay over time that can be measured by the APD detector.

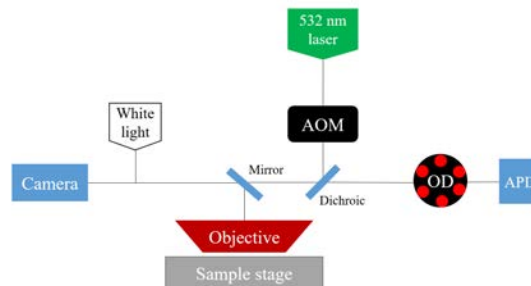


Figure 4. Simplified schematic diagram of the inverted microscope setup used for T_1 measurements.

Figure 4 is a schematic representation of the important components of the T_1 setup. The solution is held in a cuvette on the sample stage, and observed through a 5X objective. Nearby is a mirror that can be switched to direct the light either to the APD, or to a camera and accompanying white light source (which are used to focus the beam between the walls of the cuvette prior to measurement). The 532 nm LWP (long wave pass) dichroic beamsplitter allows the laser to also travel to the OD wheel and APD. The OD wheel filters out light of a certain optical density, enabling excitation at high power without damage to the detector. Lastly, near the laser source is the acousto-optic modulator (AOM), which dispatches the pulses by turning the laser on and off (it is more precise and easier to control at small timescales than the laser itself).

D. Fitting and analysis

Once the decays are obtained, they are then fit onto three models (stretch, polyexponential, and multiexponential)

$$S = I_i + C_1 \exp\left(-\left(x - T_1\right)^\beta\right)$$

$$P = I_i - C_3 \exp(-10x) + C_2 \exp\left(-\frac{x}{T_{short}}\right) + C_1 \exp\left(-\frac{x}{T_1}\right)$$

$$M = I_i + C_2 \exp\left(-\frac{x}{T_{short}}\right) + C_1 \exp\left(-\frac{x}{T_1}\right)$$

where I_i is the initial intensity, T_1 and T_{short} are the horizontal decay times, β is a measure of how similar decays of different spins are to each other, and C_1 , C_2 , C_3 are vertical amplitude measures. In two analyses the best fit is determined via reduced χ^2 values, and its coefficients are extracted; in a third analysis, only the stretch fit is used.

RESULTS AND DISCUSSION

A. Overview

The UV-Vis results aligned with expectations, with larger-sized ND samples absorbing more light; the DLS results also turned out largely as expected, despite fairly large uncertainties. The T_1 results were tested in three different analyses, due to setbacks in each iteration; in all three, a weak positive correlation between T_1 and size is observed, and the relaxation rates $1/T_1$ are favorably to semi-favorably compared with those of Tetienne *et al.* (2013).

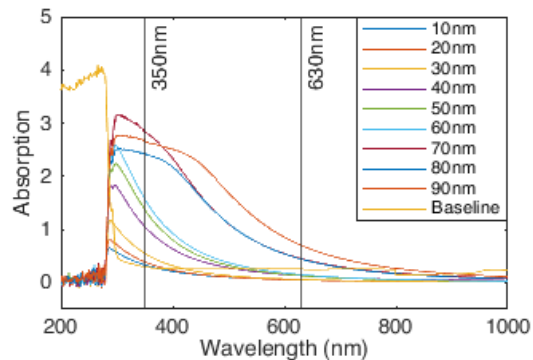


Figure 5. Absorption levels of the nine ND samples plus a DI water baseline, with the baseline values subtracted from the sample values.

B. UV-Vis results

The UV-Vis data (Figure 5) showed that the suspensions with larger NDs absorbed more visible light. This agrees with qualitative observations of the transparency of the samples (Figure 2) as well as the intuition that the greater the presence of fluorescent particles in a solution, the more light it will absorb from its surroundings. There were some unexpected results, however, such as the prominence of the 70-nm sample, which around 350 nm was significantly more absorptive than the 80- or 90-nm samples (for a clearer illustration, see Figure 19).

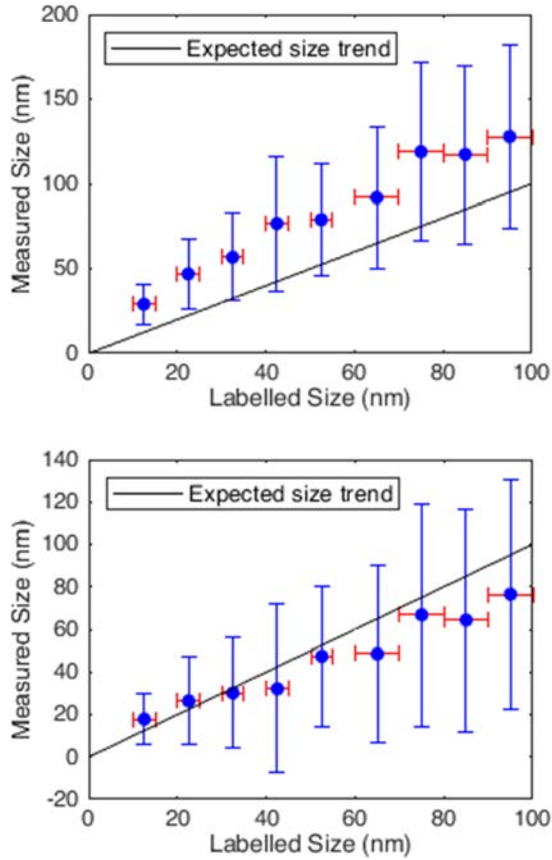


Figure 6a-b. Comparison between manufacturer-specified size and DLS-measured ND size (intensity and number, respectively).

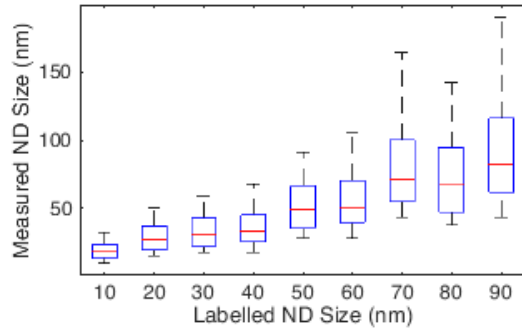


Figure 7. DLS number data in box plot form. (Uncertainties provided by the manufacturer are not depicted here.)

C. DLS results

Many of the size distribution results obtained through DLS (Figures 6 and 7) disagreed with the size range specified by the manufacturer. The intensity measurements were a consistent amount greater than this range, while the number measurements were less consistent but often below the range. In both distributions, the largest jump in estimated size is between the 60- and 70-nm samples, similarly to the largest jump in absorption in Figure 5. All the remaining plots involving measured size

use the results for number, rather than intensity, because of the overall greater certainty (as well as the choice of number in previous studies better aligning with the motivations of this project).

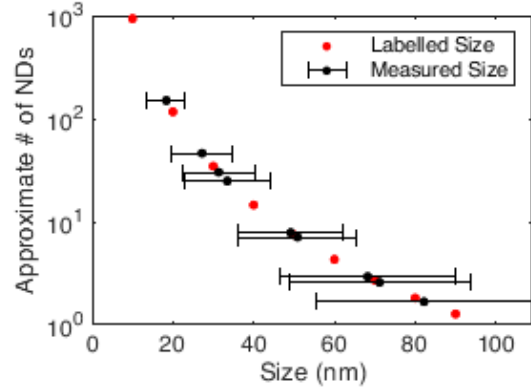


Figure 8. Estimation of ND counts probed in excitation volume, plotted as a function of ND size.

D. Estimation of ND size

Using the DLS data and some other constants, it is possible to approximate how many NDs are being probed by the laser, assuming that each diamond is perfectly spherical (Figure 8). This number was found to equal ad^{-3} , where $a \approx 9.334 \times 10^5 \text{ nm}^3$ and d is the ND diameter. This result makes physical sense because of the inverse-cubic relationship between diameter and volume in a sphere; given the fact that all the samples had the same concentration of NDs in the same total amount of solution, fewer quantities of NDs should be observed in the larger-ND samples. Despite this, the number of diamonds for some of the higher samples is lower than expected, with fewer than 5 individual NDs seemingly being probed for the 80- and 90-nm samples. (A more detailed explanation of the calculation is included in the Supplementary Material.)

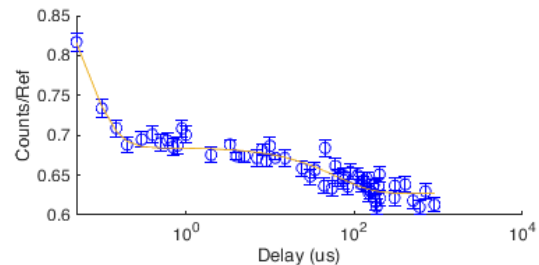


Figure 9. Example stretch exponential fit on T_1 data, for Analysis #1 (80-nm sample).

E. T_1 Analysis #1

1) Direct T_1 and size comparison

In the first analysis of the T_1 data, the best fit for all nine ND samples was the multiexponential fit. In the

example in Figure 9, T_1 controls the second, more drawn-out decay while T_{short} controls the more precipitous decay at small delay times. C_1 and C_2 control the amplitude of T_1 and T_{short} s respectively, while I_i controls the height difference between the starting and ending points of the fit. Like this example, most of the fits started at about 0.8 counts, dropped to about 0.7 by the 1 μ s mark due to the C_2/T_{short} exponential term, and then dropped past 0.65 around the 150 μ s mark due to the C_1/T_1 term. This similar behavior across different ND sizes is due to the implementation of a normalization constant (hence the y-axis being labeled as “Counts/Ref” in Figure 9).

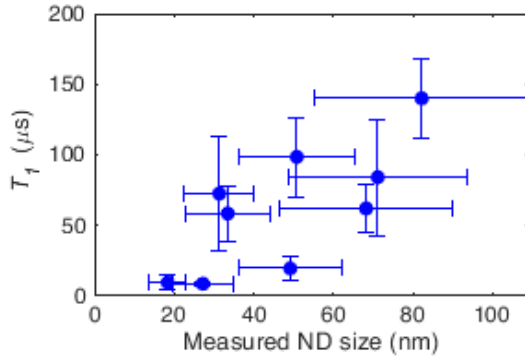


Figure 10. T_1 plotted against measured ND size, for Analysis #1.

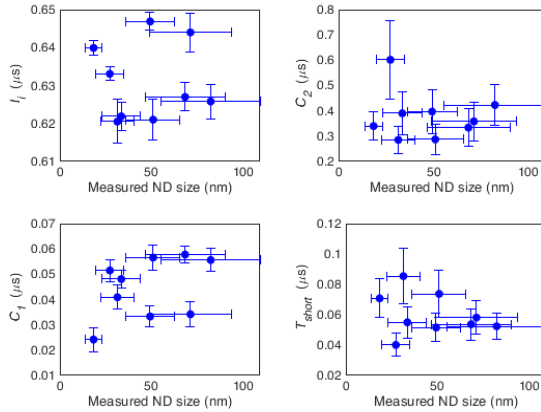


Figure 11a-d. I_i , C_2 , T_{short} and C_1 for the nine multiexponential fits from Analysis #1, plotted against ND size (clockwise from top-left).

2) Other multiexponential coefficients and size

Figure 10 shows a positive trend in T_1 as size increases, a preliminary result which, though the uncertainties are large, agrees with previous findings [4, 11, 12]. The other four parameters of the multiexponential fit were also plotted against nanodiamond size, in Figure 11. The only one of these results that might contain a significant correlation is a potential negative trend in the T_{short} graph (bottom left). To investigate this, $1/T_{short}$ was plotted against ND size (Figure 22), but no correlation was

observed. Of the two decays depicted in Figure 9, the second, longer decay (the length of which is dictated by T_1) is generally in agreement with similar studies; however, few, if any, report the existence of the sharp initial decay dictated by T_{short} [4, 11, 13]. For most of the multiexponential fits, this decay almost completely disappears when the leftmost data points are ignored. Thus, the decay is most likely an artifact due to a mistiming between the laser and the detector, with the APD potentially capturing a previous pulse in the sequence and therefore delivering an inaccurate measurement. To better capture T_1 behavior, a new analysis (Analysis #2; see part F of this section) is needed, ignoring the readings at short delay times.

3) Relaxation rate vs. size; comparison to Tétienne et al.

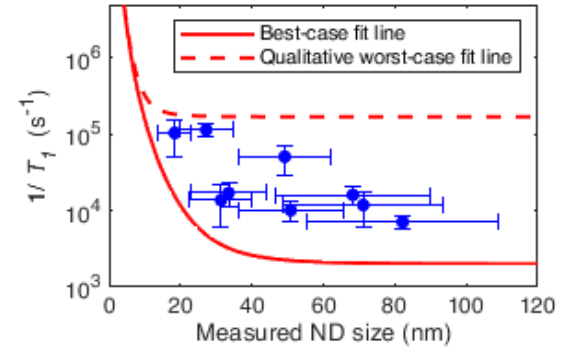


Figure 12. Relaxation rate $1/T_1$ (from Analysis #1) plotted against measured ND size, with a “best-case” and “worst-case” decay rate adapted from Tétienne *et al.* (2013).

Tétienne *et al.* (2013) plot their relaxation rates against nanodiamond size, along with models for a “best-case” and “worst-case” scenario (Figure 23). These models assume the ND is a sphere; the best case is where the NV is located in the sphere’s center, while the worst case is where the NV is located about 3 nm from the surface [4]. (This surface distance is close to the NV’s photostability limit, meaning that bringing it any closer would likely cause it to undergo a molecular change as a result of exposure to light.) Here, the best-case model is replicated in detail while the worst-case model, requiring significantly more computation, is qualitatively transcribed.

Tétienne *et al.*’s best-case model is the relation

$$\frac{1}{T_1} = \frac{1}{T_1^{bulk}} + \frac{3\gamma_e^2 B_{\perp}^2}{R \left(1 + \frac{\omega_0^2}{R^2}\right)}$$

where T_1^{bulk} is the T_1 time of bulk diamond, γ_e is the electron gyromagnetic ratio, R is the fluctuation rate of the spins at the diamond surface, and ω_0 is the NV’s electron spin resonance (ESR) frequency. B_{\perp}^2 is the variance of the transverse magnetic field at the NV’s location, itself a function of the nanodiamond’s diameter d [4]. Using a

combination of literature values and values computed by Tetienne *et al.*, this equation was plotted in Figure 12 as

$$\frac{1}{T_1} = 2000 + \frac{b}{d^4}$$

where $b \approx 1.549 \times 10^9$. Tetienne *et al.* argue that the d^{-4} dependence of the relaxation rate is due to spin-spin interactions integrated over a surface, a value proportional to d^{-6} ; this is the underlying reason for relaxation rates increasing as ND size decreases. (More details about the calculation of this model can be found in the Supplementary Material.)

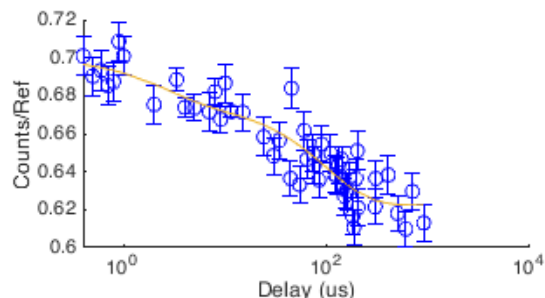


Figure 13. Example stretch exponential fit on T_1 data, for Analyses #2 and #3 (80-nm sample).

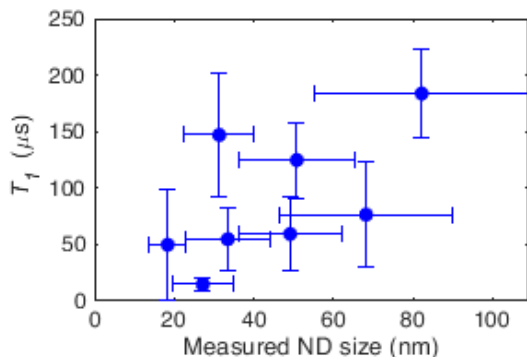


Figure 14. T_1 plotted against measured ND size, for Analysis #2.

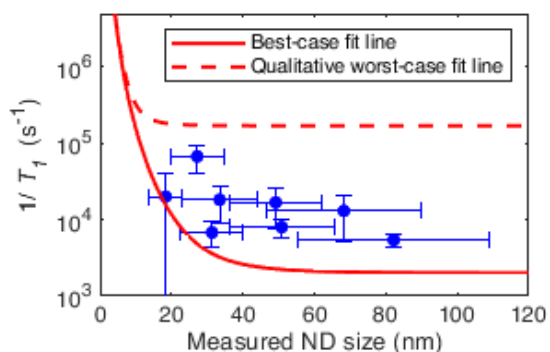


Figure 15. Relaxation rate $1/T_1$ (from Analysis #2) plotted against measured ND size, with a “best-case” and “worst-case” decay rate adapted from Tetienne *et al.*

F. T_1 Analysis #2

As stated above, a new analysis is needed when ignoring extremely short delay times, so Analysis #2 repeats parts 1) to 3) above from Analysis #1, except it additionally imposes a threshold at a delay time of 300 nanoseconds. The expectation was that by eliminating the high-count, low-delay time data, the fits would be more linear in the 1-10 microsecond range, like a stretch exponential (as Figure 13 illustrates). However, this only occurred for three of the nine sizes (40, 70, and 80 nm); four sizes were still best fit by the multiexponential model, and two by the polyexponential model. Like in Figure 9, the normalized fits were relatively similar to each other. Comparison of T_1 across these different models can still be done; the result is plotted against size in Figure 14, which displays the same general trend as Figure 10. (A full coefficient comparison like Figure 11 is no longer relevant.) Similarly, the model of Tetienne *et al.* is also compared in Figure 15. The data points along the decay seem to be slightly closer to the best-case line than in Figure 12, and slightly less vertically disjointed.

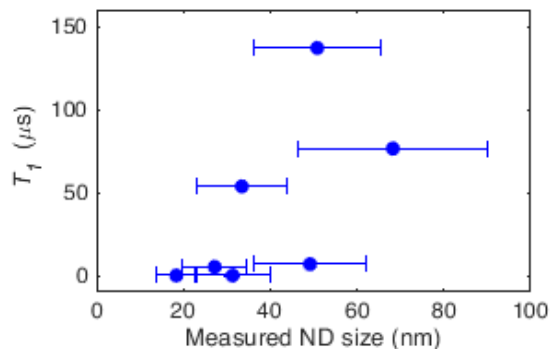


Figure 16. T_1 plotted against measured ND size, for Analysis #3.

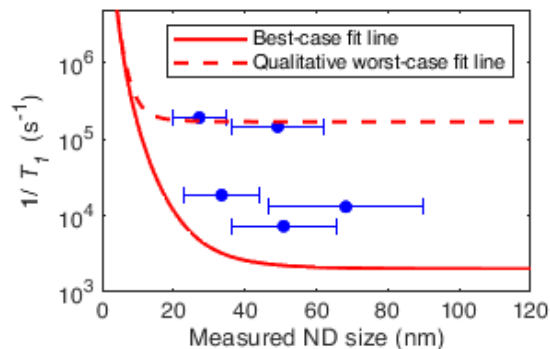


Figure 17. Relaxation rate $1/T_1$ (from Analysis #3) plotted against measured ND size, with a “best-case” and “worst-case” decay rate adapted from Tetienne *et al.*

G. T_1 Analysis #3

The aforementioned unexpected variation in model selection motivates a third analysis, in which the stretch exponential fit is manually selected for all nine sizes. As seen in Figures 16 and 17, some data is omitted as a result, with a few T_1 data points being several orders of magnitude higher than those of the previous analyses. (In Figure 17, for example, there are two data points well outside of the range of both Tetienne *et al.* models, with a relaxation rate of roughly 10^8 s⁻¹.) Another drawback to these results is the very small uncertainty in the T_1 results. This indicates some sort of inaccuracy in error generation or propagation, especially when comparing with the error bars from previous analyses.¹ The data that does remain, however, is in line with the first two analyses, showing a positive correlation between T_1 and size (if not a very strong one) in Figure 16, and a somewhat smooth decay near the best-case line for a few data points in Figure 17.

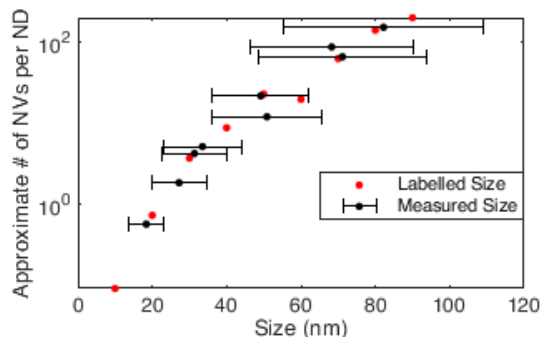


Figure 18. Approximate number of NV centers per ND plotted against labelled and measured ND size. Details for this calculation can be found in the Supplementary Material.

H. General analysis remarks

The fact that three different analyses all report a similar positive trend between T_1 and ND size is encouraging, even though no significant underlying changes have been made from analysis to analysis. In all three comparisons with Tetienne *et al.*, the data mostly falls between the best- and worst-case models (though admittedly this window is somewhat generous, spanning a few orders of magnitude). Ideally, the data points would follow a fairly smooth curve, and not display too much vertical variation from that curve. This is because though Tetienne *et al.* attempt to measure single spins inside NDs, the research here has been done with ensembles of spins, meaning that more NV data is being collected. (Figure 18 shows that many of the samples appear to contain tens or even hundreds of NVs per ND.) Thus, it was expected that the increased amount of data would more accurately

¹ This might have also been an issue for the most extreme errors seen in Figure 15.

explain the behavior of the system (i.e. an average of hundreds or thousands of data points is more reliable than an average of tens). Though Analysis #2 was relatively smooth in this regard, some questions still remain to be answered regarding this single-spin versus spin-ensemble dichotomy.

CONCLUSION

A. Summary of results

This research project aimed to contrast nanodiamonds of different sizes in terms of light absorption, size distribution, and spin relaxation times. The UV-Vis and DLS measurements generally aligned with expectations, overall confirming the NDs' size as labelled, and showing that larger NDs were more absorptive; however, some anomalies and broad standard deviations were present. The relaxation rates $1/T_1$ were successfully fitted to multiple exponential models, and found to decrease over time, in agreement with the results of Tetienne *et al.* (2013). However, the goal of replicating those results with less uncertainty remained unmet, particularly in terms of size; there also remain several unanswered questions that have arisen throughout the research process.

B. Improvements and extensions

Of immediate interest for further investigation is thoroughly examining and optimizing the choice of the "best fits" in the analysis; there were a lot of unexplained hiccups in how the coefficients were generated (hence missing data points in Analyses #2 and #3). Furthermore, the reduced χ^2 statistic might not have been as useful to selecting an optimal fit as some other information criterion. For example, there were many instances where χ^2 was less than one, indicating overfitting, and fits that had decent χ^2 values sometimes produced extreme, physically unintuitive T_1 values. (χ^2 values for all three analyses can be found in Figure 21.) Going into detail in how the fits themselves are generated might be worthwhile as well, in case there is a more systemic problem that has as yet been unobserved.

It would also be useful to redo the calculations carried out by Tetienne *et al.* for the coefficients in the best-case model, in a manner more tailored to this setup. For example, Tetienne *et al.*'s use of single spins might have led to different constraints on the system than this research, which used spin ensembles. A more rigorous generation of the worst-case model (which was replicated only visually) would also be valuable.

Another improvement to the experiment would be a second analysis of the T_1 results, but using the intensity measurements from the DLS data, rather than the number measurements. Though the decision of which DLS result to use varies based on the process and outcome of the research (counting-based techniques and microscopy, both

of which are utilized heavily in this research, are often best accompanied by number-based light scattering data), the intensity measurement is generally purer and more comprehensive [14]. Therefore, rerunning the analyses and comparison with the results of Tetienne *et al.* would be useful in confirming (or perhaps disproving) the results presented above.

Other methods of measuring ND size could be used in lieu of DLS; for example, Tetienne *et al.* use atomic force microscopy (AFM), while Shulevitz *et al.* apply a combination of AFM, DLS, and manufacturer specifications [7].

Lastly, Tetienne *et al.* (2013) compare T_1 not only against ND size but also against magnetic environment. They introduce a magnetic perturbation to the system by coating the diamond surface with a gadolinium perchlorate solution, which contains paramagnetic Gd^{3+} ions. (The choice of gadolinium is motivated by its use as a contrast agent in MRI.) Tetienne *et al.* find that NDs decorated with Gd^{3+} have higher $1/T_1$ rates than untreated NDs; using that result, they finally calculate the sensitivity of a single NV center to its magnetic surroundings, obtaining a rough estimate of 14 electron spins [4]. Replicating this process with the diamonds and setup used here would be another potential next step, though with a larger scope of spins it may not be as useful for nanoscale magnetic imaging.

C. Sensing applications and outlook

As discussed, the properties of NV centers in fluorescent NDs are of particular interest for biosensing, due to their ability to optically read out small numbers of spins in an environment. One example of this is using spin relaxometry to map free radicals in pathogens that escape phagocytosis, in order to better understand the failures of the bacteria-killing mechanism [13]. There still remain challenges to broad biomedical use of NV centers, such as the need to improve sensitivity at miniature scales, and considerations of how the NVs will practically be implemented in real biomedical situations [6]; but investigating and developing existing or new materials is a useful way of addressing those needs. This project has given some new insight into how spin relaxometry depends on factors like particle size; by pointing researchers towards the optimal qualities a biosensing system might have, it represents a small step towards achieving that ultimate goal.

SUPPLEMENTARY MATERIAL

A. ND number and NV-per-ND calculations

The calculation of how many NDs are in each sample involves finding the number of NDs per milliliter of water and multiplying it by the volume probed by the laser. The former amount is computed by dividing the diamond's concentration (1 mg/mL) by both the density of diamond

(3.53 g/cm³) and the volume of a sphere ($\pi d^3/6$). The latter amount is approximated as a cylinder, whose diameter is the Gaussian beam waist w_0 and whose length is the Rayleigh range z_R . These two constants can themselves be computed via the following formulae

$$NA = \frac{\lambda}{\pi w_0} \quad z_R = \frac{\pi w_0^2 n}{\lambda}$$

where NA is the numerical aperture of the lens used (0.15 for this setup), λ is the light's wavelength (532 nm), and n is the sample's index of refraction (assumed to be that of water, 1.33, for this calculation). This last assumption is indeed a limitation of the model: the higher-sized samples most likely do have a different index of refraction due to being less transparent than the lower-sized ones (as seen in Figure 2), so the excitation volume might have to be modified to accommodate this.

The calculation of number of NV centers per ND also involved assuming a spherical ND in order to convert volume to number, but also used the concentration of NVs per ND, as specified by the manufacturer in parts per million, and the atomic density of diamond. This last constant was found by dividing the number of atoms in a unit cell of diamond (8) by the volume of the unit cell (which is a cube with a side length of 3.567 Å).

B. Best-case model calculation

Assuming the surface density of spins to be $\sigma = 1$ nm⁻² (typical of these systems), Tetienne *et al.* calculate B_{\perp} to be 26 mT nm⁻³ times d^{-4} . They also calculate the total fluctuation rate by decomposing it into fluctuations caused by dipolar coupling and intrinsic vibrational spin relaxation (R_{dip} and R_{vib} , respectively), such that $R = R_{\text{dip}} + R_{\text{vib}}$. Using the same σ as above, they calculate $R_{\text{dip}} = 11$ ns⁻¹; based on existing electron paramagnetic resonance (EPR) studies finding R_{vib} to be 1 ns⁻¹ or less, they ignore the vibrational component and assume $R \approx R_{\text{dip}}$. Lastly, they assume a T_1^{bulk} value of 2 ms [15].

All components of the above process were maintained in replicating the best-case fit. The remaining values in the model, which are taken from the literature, are the electron gyromagnetic ratio, $\gamma_e = 1.76 \times 10^{11}$ s⁻¹ T⁻¹, and the NV ESR frequency, $\omega_0 = 2\pi D$ (where $D = 2.87$ GHz is the zero-field splitting of diamond).

C. Supplementary figures

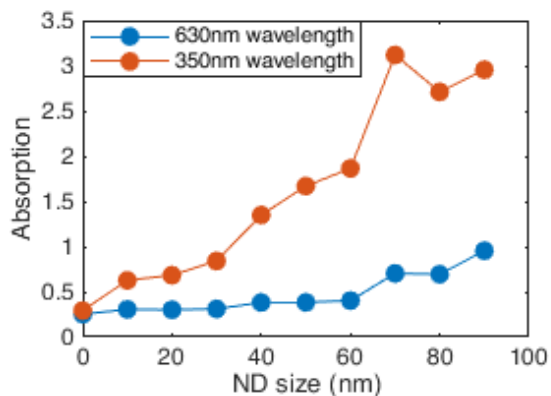


Figure 19. Absorption values extracted at wavelengths of 630 nm and 350 nm. The 630 nm values were used for DLS measurements, while the 350 nm values illustrate how the result from the 70-nm sample is an outlier compared to the rest of the data. Baseline values have not been subtracted.

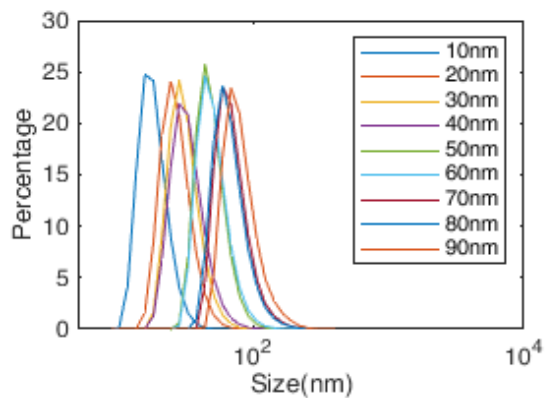
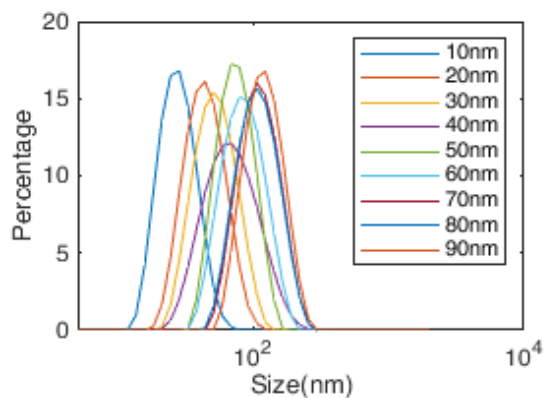


Figure 20a-b. Raw intensity and number measurements from DLS. The data consists of size bins of measurements, along with percentages of how frequently each bin is selected.

ND size	Reduced χ^2	ND size	Reduced χ^2
10 nm	1.0624	60 nm	1.5590
20 nm	0.8866	70 nm	1.8007
30 nm	1.8837	80 nm	1.5026
40 nm	1.1977	90 nm	1.5601
50 nm	1.1127		
10 nm	0.895	60 nm	1.4734
20 nm	0.8821	70 nm	1.7759
30 nm	1.3737	80 nm	1.2749
40 nm	1.0215	90 nm	0.9702
50 nm	0.9925		
10 nm	0.9376	60 nm	1.5214
20 nm	0.884	70 nm	1.8134
30 nm	1.5645	80 nm	1.3019
40 nm	1.0427	90 nm	1.2316
50 nm	1.0224		

Figure 21. Reduced χ^2 values of the fits used for each sample for Analyses #1, #2, and #3.

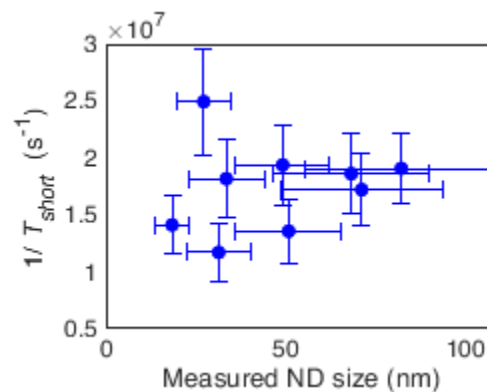


Figure 22. $1/T_{short}$ (Analysis #1) plotted against measured ND size.

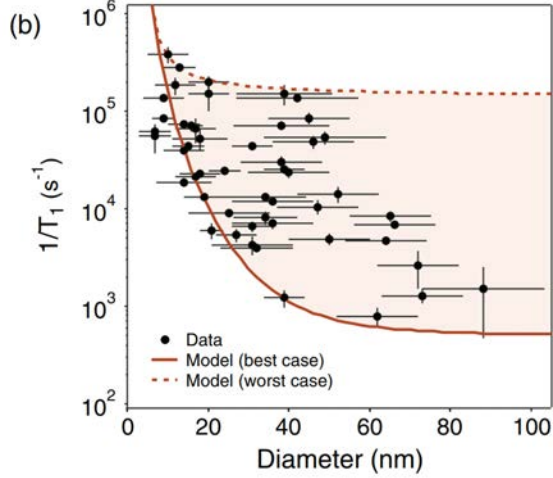


Figure 23. Copy of Figure 2(b) from Tetienne *et al.* (2013), which plots relaxation rate against diamond size along with two extreme models taking into account NV location within the ND.

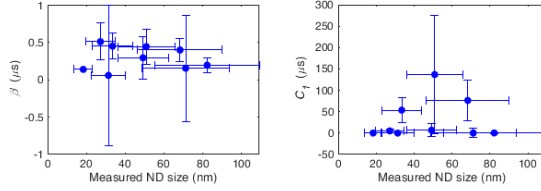


Figure 24a-b. β and C_1 as a function of ND size for Analysis #3. No strong correlation is observed. The large uncertainties are possibly due to error in generating the fit and uncertainty.

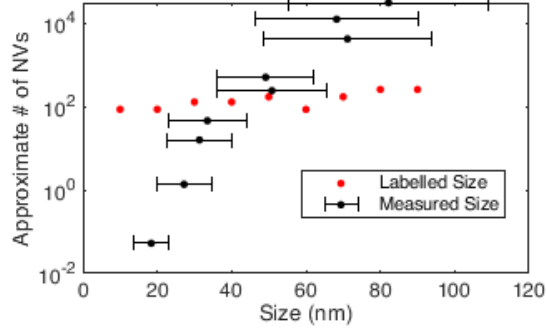


Figure 25. Approximation of the number of NV centers probed in the excitation volume. This number is essentially a product of the number of NDs probed in the excitation volume (Figure 8), and the number of NVs per ND (Figure 18). A linear or constant relationship was hypothesized, due to the $1/d^3$ dependence in the former curve and the d^3 dependence in the latter curve cancelling each other out. This expectation was mostly realized here for the labelled ND sizes, but not so much for the measured sizes, perhaps due to an imbalance in the coefficients.

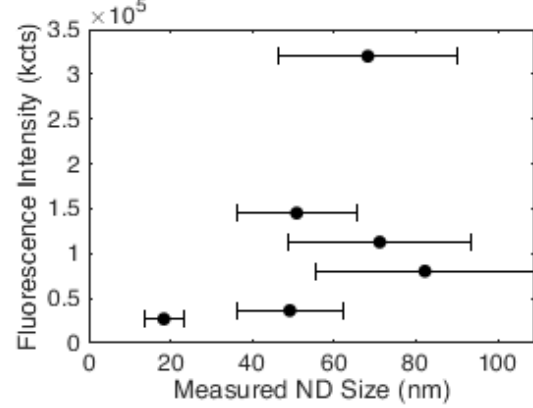


Figure 26. Plot of fluorescence intensity against measured ND size for some samples. The optical density formula is

$$OD = \log_{10}\left(\frac{I_0}{I_t}\right)$$

where I_0 is the reflected intensity and I_t is the transmitted intensity. I_t was recorded by the APD detector prior to each T_1 measurement, and the setup includes an adjustable OD wheel (see Figure 4) whose settings were also recorded. Thus, it is possible to solve for I_0 (essentially the sample's measured intensity before the light hits the OD wheel) and plot it against size. No strong correlation was observed.

ACKNOWLEDGEMENTS

The authors would like to thank the National Science Foundation for financial support of the SUNFEST program, through Grant No. 1950720; Henry J. Shulevitz and the Quantum Engineering Lab for assistance with and use of the T_1 setup; Cherie Kagan, Andrew Tsourkas, Ahmad Amirshaghghi, Chavez Lawrence, and Jonah Ng for assistance with the DLS and UV-Vis equipment; Olga Shenderova, Mary Eberle, and Carol Heffer for assistance with the nanodiamond samples; John Kehayias for writing support, and Sue Ann Bidstrup Allen and Tiko Mkhaidze for administrative support.

REFERENCES

- [1] Awschalom, D. D. *et al.* Quantum spintronics: engineering and manipulating atom-like spins in semiconductors. *Science* 339, 1174-1179 (2013).
- [2] Acosta, V. and Hemmer, P. Nitrogen-vacancy centers: physics and applications. *MRS Bulletin* 38, 127-130 (2013).
- [3] Childress, L. *et al.* Atom-like crystal defects: from quantum computers to biological sensors. *Phys Today* 67 (10), 38-43 (2014).
- [4] Tetienne, J.-P. *et al.* Spin relaxometry of single nitrogen-vacancy defects in diamond nanocrystals for magnetic noise sensing. *Phys Rev B* 87, 235436 (2013).
- [5] Schirhagl, R. *et al.* Nitrogen-vacancy centers in diamond: nanoscale sensors for physics and biology. *Annu Rev Phys Chem* 65, 83-105 (2014).
- [6] Aslam, N. *et al.* Quantum sensors for biomedical applications. *Nat Rev Phys* 5, 157-169 (2023).

- [7] Shulevitz, H. J. *et al.* Template-assisted self-assembly of fluorescent nanodiamonds for scalable quantum technologies. *ACS Nano* 16, 2, 1847–1856 (2022).
- [8] Rendler, T. *et al.* Optical imaging of localized chemical events using programmable diamond quantum nanosensors. *Nat Commun* 8, 14701 (2017).
- [9] Hsiao, W. W.-W. *et al.* Fluorescent nanodiamond: a versatile tool for long-term cell tracking, super-resolution imaging, and nanoscale temperature sensing. *Chem Res* 49, 3, 400–407 (2016).
- [10] Stetefeld, J. *et al.* Dynamic light scattering: a practical guide and applications in biomedical sciences. *Biophys Rev* 8, 4, 409-427 (2016).
- [11] Perona Martínez, F. *et al.* Nanodiamond relaxometry-based detection of free-radical species when produced in chemical reactions in biologically relevant conditions. *ACS Sens* 5, 12, 3862-3869 (2020).
- [12] Rej, E. *et al.* Hyperpolarized nanodiamond with long spin-relaxation times. *Nat Commun* 6, 8459 (2015).
- [13] Wu, K. *et al.* Diamond relaxometry as a tool to investigate the free radical dialogue between macrophages and bacteria. *ACS Nano* 17, 2, 1100-1111 (2023).
- [14] Nobbmann, U. and Morfesis, A. Light scattering and nanoparticles. *Mater Today* 12, 5, 52-54 (2009).
- [15] Jarmola, A. *et al.* Temperature- and magnetic-field-dependent longitudinal spin relaxation in nitrogen-vacancy ensembles in diamond. *Phys Rev Lett* 108, 197601 (2012).